The Effect of Boundary Layer Character on Stochastic Rotor Blade Vortex Shedding Noise

Christopher S. Thurman
christopher.thurman@nasa.gov
Research Aerospace Engineer
NASA Langley Research Center
Hampton, VA, USA

Nikolas S. Zawodny
nikolas.s.zawodny@nasa.gov
Research Aerospace Engineer
NASA Langley Research Center
Hampton, VA, USA

Nicole A. Pettingill
nicole.a.pettingill@nasa.gov
Research Aerospace Engineer
NASA Langley Research Center
Hampton, VA, USA

ABSTRACT

This work illustrates the effect of a rotor blade's boundary layer on the broadband laminar boundary layer vortex shedding (LBL-VS) self-noise emitted from an optimum hovering rotor through experimental and multifidelity computational studies. Blade surface roughness effects associated with different manufacturing techniques and the effect of adding a boundary layer trip were shown to decrease LBL-VS noise by upwards of 30 dB at the frequency of maximum emission with a slight penalty in aerodynamic performance when compared with smooth rotor blades. Low-fidelity 2-D viscous flow analysis verified the presence of laminar separation bubbles on the rotor blades, which are responsible for LBL-VS noise. Three high-fidelity lattice-Boltzmann simulations were conducted with different wall-functions to predict the boundary layer character correspondent to their experimental counterpart and the resultant presence or absence of LBL-VS noise. Excellent aerodynamic and aeroacoustic agreement was seen between the lattice-Boltzmann simulations and the experimental data for the cases with surface roughness and the boundary layer trip. The broadband noise results from the simulation with fully turbulent wall-functions diverged from the experimental results above 5 kHz. The transitional wall-function simulation, which emulated the smooth experimental blades, underpredicted thrust by 14% and broadband noise by a minimum of 10 dB with an accurately predicted broadband noise trend.

NOMENCLATURE

a	Fluid speed of sound, in/s
$c(r)$	Rotor chord length distribution, in
c_r	Chord length at the r spanwise location, in
c_{tip}	Rotor chord tip length, in
C_f	Skin friction coefficient
C_T	Thrust coefficient, $\frac{T}{\rho A(\Omega R)^2}$
C_μ	Model coefficient for turbulent viscosity
$\mathbf{e}_i$	Particle convective speed along the i^{th} direction
f_i	Particle velocity distribution function along the i^{th} direction
f_i^{eq}	Particle equilibrium distribution along the i^{th} direction
FSTI	Freestream turbulence intensity
k	Turbulent kinetic energy, in^2/s^2
N_b	Number of rotor blades
N_{crit}	Critical transition amplification factor
p_{ref}	Reference pressure, 20 μPa
PSD	Power spectral density, dB/Hz
P_{xx}	Power spectral density, Pa^2/Hz
r	Normalized span location, $\frac{x}{R}$
R	Rotor radius, in
Re_r	Reynolds number at the r spanwise location
SPL	Sound pressure level, dB
$\text{SPL}_{1/3}$	One-third octave sound pressure level, dB
U_{fric}	Friction velocity, in/s
$\mathbf{x}$	Particle position, in
y	Radial observer location relative to center of rotor rotation, ft
y^+	Normalized wall distance
α_0	Airfoil zero lift angle of attack, rad
Δf	Narrowband spectra frequency resolution, Hz
Δs	Finest voxel size, in
ε	Turbulent kinetic energy dissipation rate, in^2/s^3
ν	Kinematic fluid viscosity, in^2/s
$\theta_{tw}(r)$	Rotor twist distribution, rad
θ_0	Collective pitch, deg
Θ_{obs}	Observer angle relative to rotor plane, deg
ρ	Fluid density, lb/in^3
$\sigma(r)$	Rotor solidity distribution, $\frac{N_b c(r)}{\pi R}$
τ	Viscous relaxation time, s
τ_{eff}	Recalibrated relaxation time, s
τ_{wall}	Wall shear stress, lb/in^2
ω_i	Weight function in the i^{th} direction
Ω	Rotor rotational rate, revolutions per minute (RPM)
Ω_i	Bhatnagar-Gross-Krook collision operator

Presented at the Vertical Flight Society's 78th Annual Forum & Technology Display, Fort Worth, TX, May 10–12, 2022.

INTRODUCTION

Airfoil tonal noise has been studied both experimentally in Refs. 1–4 and computationally in Refs. 5–7, for fixed, symmetric NACA airfoils. These tones are caused by an acoustic feedback mechanism between laminar separation bubbles in the boundary layer and the correspondent vortices traversing the airfoil trailing edge. An illustration of this phenomena can be seen in Fig. 1.

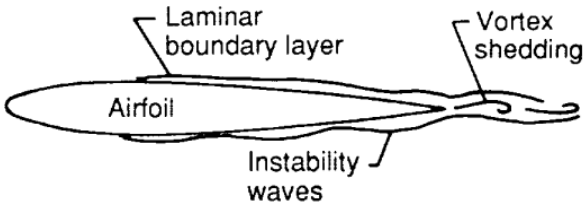

Figure 1: Illustration of laminar boundary layer vortex shedding (LBL-VS) noise. Apdated from Brooks et al. (Ref. 8).

This type of noise has been shown to occur for NACA 0012 airfoils at chord-based Reynolds numbers ranging from approximately 5 x 10^4 to 2 x 10^6 over angles of attack up to 8 degrees (Ref. 4). This noise source is tonal in a 2-D sense, respective of the airfoil vortex shedding frequency; however, in the context of rotorcraft, this noise source is independent of the blade passage frequency (BPF). By definition, this type of noise is a form of broadband self-generated noise in rotating systems, which is commonly referred to as laminar boundary layer vortex shedding (LBL-VS) noise for rotorcraft applications. Broadband LBL-VS noise was shown by the authors to occur for a canonical small unmanned aerial system (sUAS) rotor over a wide range of operating conditions (Ref. 9). This noise, however, was only present for rotor blades fabricated using stereolithography (SLA) and was absent for rotor blades fabricated using selective laser sintering (SLS). The SLS blades had a noticeable surface roughness when compared to the SLA blades, and it was presumed that the SLS blade's surface roughness generated a turbulent boundary layer over the rotor blades, effectively eliminating LBL-VS noise (Ref. 3). A computational study was also performed by the authors in Ref. 10 on the same canonical sUAS rotor geometry. In this study, high-fidelity lattice-Boltzmann simulations were compared to low-fidelity simulations using the semiempirical self-noise prediction methodology devised by Brooks et al. (BPM model) in Ref. 8 and implemented in ANOPP2's (Ref. 11) Self-Noise Internal Functional Module (ASNIFM). This computational study showed that the BPM model required the addition of a Reynolds number limit to correct the predicted frequency of LBL-VS noise and that the LBL-VS noise amplitude was overpredicted. The lattice-Boltzmann simulations showed that LBL-VS noise was generated at approximately 80% of the blade span. They also showed that there was turbulent flow on the pressure side of the blades caused by a blade wake interaction (BWI) event, where the turbulence entrained in the tip vortex of a preceeding blade traversed the surface of a downstream blade, possibly having an effect on the LBL-VS noise.

This work illustrates the effect of the rotor blade's boundary layer on LBL-VS noise through experimental and multi-fidelity computational studies. Experimental testing was performed using rotor blades fabricated using different additive manufacturing techniques to show the effect of surface roughness on the presence of LBL-VS noise. A boundary layer trip was added to the blades to present an LBL-VS mitigation strategy and to compare the aerodynamic performance and acoustic attributes of this tripped condition to untripped cases. A computational strategy was also employed to determine the presence of laminar separation bubbles responsible for LBL-VS noise from a 2-D perspective and also to simulate the rotor under natural transition, turbulent, and tripped flow conditions.

TECHNICAL APPROACH

Rotor Design

The rotor utilized in this work was a two-bladed ($N_b = 2$) rotor with a radius of $R = 7.5$ in designed using blade element momentum theory (BEMT) to perform optimally in hover conditions. This 'optimum hovering rotor,' shown in Fig. 2, was designed to produce 1.875 lb of thrust at $\Omega = 3950$ RPM using the twist distribution, $\theta_{tw}(r)$, from Eq. (1) and the chord distribution, $c(r)$, shown in Eq. (2) (Ref. 12):

$$\theta_{tw}(r) = \frac{1}{r}\left(\frac{4C_{T_{\text{design}}}}{5.73\sigma(r)} + \sqrt{\frac{C_{T_{\text{design}}}}{2}}\right) - \alpha_0, \tag{1}$$

where r is the normalized span location, $C_{T_{\text{design}}}$ is the thrust coefficient calculated using the design thrust value of 1.875 lb, $\sigma(r)$ is the spanwise distribution of rotor solidity, and α_0 is the zero lift angle of attack of the airfoil. For the chord distribution:

$$c(r) = \frac{c_{\text{tip}}}{r}, \tag{2}$$

where c_{tip} is the chord length at the blade tip, which was 0.75 in.

Figure 2: Optimum hovering rotor geometry.

An optimum hovering rotor can be defined as one that has both minimal induced power requirements and minimal profile power requirements. Equation (1) is such that the rotor induces uniform inflow, satisfying the induced power requirement, and Eq. (2) allows each radial station to operate at an optimal lift to drag ratio, which satisfies the profile power requirement. Since the optimum chord distribution from Eq. (2) is not physically realizable, a linear taper ratio of 2.25 to 1 was selected for this work. This linear taper ratio was thought to best replicate the taper of an optimum hovering rotor over the outboard 25% span of the rotor, as shown in Fig. 3. A cambered NACA 5408 airfoil profile with $\alpha_0 = -4.84°$ was used along the span of the blades, which had a trailing edge thickness equivalent to 3% of the blade's chord length at each spanwise location. This selection was made using aerodynamic and aeroacoustic prediction models devised by the authors in Ref. 13.

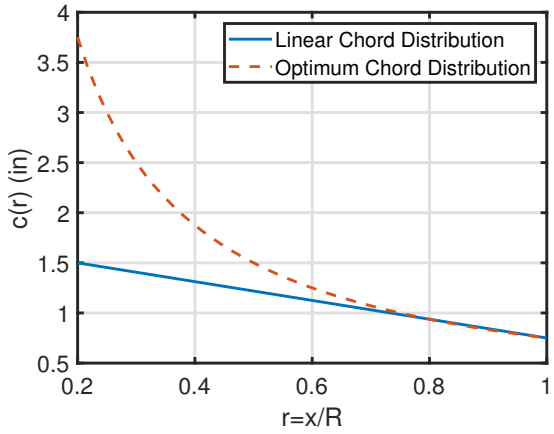

Figure 3: Comparison of 2.25 to 1 linear taper ratio to the taper ratio of an optimum hovering rotor.

Three rotors consisting of different blade types were used in this study: the first rotor used blades fabricated from smooth SLA material, the second rotor utilized these same SLA blades; however, a boundary layer trip consisting of 0.01-inch glass beads was adhered to each blade's quarter chord location along the suction side of the blade, and the third rotor used blades fabricated from SLS material, which had a noticeable surface roughness. The second and third blade types are shown in Figs. 4a and 4b, respectively, for clarity. The first and third blade types were representative of cases with and without LBL-VS noise, respectively, and the second blade type served as an LBL-VS mitigation technique. These blade types will hereby be referred to as SLA-smooth, SLA-tripped, and SLS, respectively.

Experimental Setup

Experimental testing was conducted in the Small Hover Anechoic Chamber (SHAC) facility at the NASA Langley Research Center. The SHAC is acoustically treated down to 250 Hz and has working dimensions of 12.70 ft x 8.40 ft x 10.70 ft. The suitability of this facility for testing small rotors in static hover conditions was shown in Refs. 9 and 14 when flow recirculation is properly addressed. Two mesh screens of open areas 72% and 51% were placed 4.2 and 7.5 rotor radii, respectively, downstream from the rotor to reduce recirculation effects. A Brüel & Kjær (B&K) LAN-XI data acquisition (DAQ) module and B&K Connect software system were used for data acquisition. Eight B&K Type 4939 free-field microphones are located in the upper corner of the SHAC, and span a range of $\Theta_{obs} = +38°$ above the plane of the rotor to $\Theta_{obs} = -49°$ below the plane of the rotor, as shown in Fig. 5. These microphones are located at a minimum of 10 rotor radii away from the rotor, which is in the acoustic far-field. A laser sensor tachometer located directly below the rotor was used to monitor the rotation rate of the rotor, and a 6-component ATI-IA Mini40 multiaxis load cell was used to measure the aerodynamic forces. The rotor was powered using a KDE Direct 3510XF 475 KV brushless motor and a Maytech 40A OPTO electronic speed controller.

(a) SLA-tripped blades with adhered boundary layer trip.

(b) SLS blades with noticeable surface roughness.

Figure 4: Photographs of blade surfaces.

Low-Fidelity Tools

The multifidelity computational strategy used in this work consisted of two parts. The first part used the 2-D viscous flow prediction tool, XFOIL, to verify the presence of laminar separation bubbles for an NACA 5408 airfoil with a sharp trailing edge. Viscous 2-D airfoil predictions were generated for operating conditions at the $0.75R$ and $0.95R$ spanwise locations of the rotor. This decision was based on LBL-VS noise

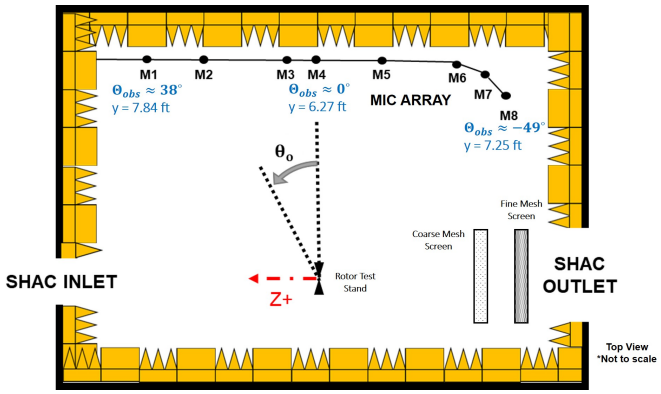

Figure 5: SHAC acoustic measurement configuration.

being predicted at the $0.80R$ spanwise location for a similar canonical rotor (Ref. 10) and the fact that there is an effective blade area responsible for thrust generation correspondent to approximately 95% - 98% of the blade span due to tip vortex formation (Ref. 12). The flow conditions at these two spanwise locations are shown in Table 1 with angle of attack values generated using ANOPP's Propeller Analysis System (PAS) (Ref. 15) at the $\Omega = 3950$ RPM operating condition. Since XFOIL uses the e^N transition method, a critical transition amplification factor, $N_{crit} = 9$ was used, which is correspondent to a freestream turbulence intensity (FSTI) of 0.07%. This FSTI value was calculated using the following relation proposed by Mack (Ref. 16):

$$N_{crit} = -8.43 - 2.4 \ln(\text{FSTI}). \tag{3}$$

High-Fidelity Tools

The second part of this computational effort entailed the use of the lattice-Boltzmann method very-large-eddy simulation (LBM-VLES) software, PowerFLOW 6-2021, to conduct three rotor simulations at the design operating condition of $\Omega = 3950$ RPM. PowerFLOW utilizes wall-functions in the first volumentric cell adjacent to the rotor geometry to approximate the boundary layer. A detailed discussion of these wall-functions will be given in the next section. Generally speaking, the sofware allows for the specification of three wall-function types: fully laminar, fully turbulent, or transitional; the latter two of which were utilized in this work. The first simulation, which will be referred to as the natural transition (NT) case, used the transitional wall-functions to capture the naturally occuring boundary layer transition from the SLA-smooth blades and predict LBL-VS noise. The second simulation, referred to as the physical trip (PT) case, entailed physically modeling the boundary layer trip from the SLA-tripped case at the quarter chord location along the span of the blades' suction sides, as shown in Fig. 6. This modeled boundary layer trip began at the quarter chord location, had a chordwise length of 0.04 in, a height of 0.004 in, which was thought to be representative of the root mean square of the physical boundary layer trip height on the SLA-tripped blades, and traversed the outer 70% of the blade span. This second simulation used turbulent wall-functions downstream of the boundary layer trip on the blades' suction sides and transitional wall-functions elsewhere.

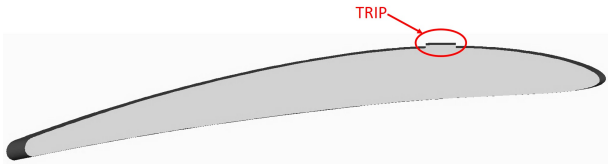

Figure 6: Physical modeling of the boundary layer trip along the span of a blade suction side.

Lastly, the third simulation, referred to as the fully turbulent (FT) case, utilized turbulent wall-functions over the entirety of the blades to model the SLS blades, which were absent of LBL-VS noise due to the presence of a turbulent boundary layer. Unsteady surface pressure data from the simulations were then used within the software, PowerACOUSTICS 6-2021, to calculate the propagated acoustic pressure time history (APTH) at defined observer locations using Farassat's formulation 1A (F1A) (Ref. 17) solution to the Ffowcs Williams and Hawkings (FW-H) acoustic analogy (Ref. 18).

Lattice-Boltzmann Methodology

The lattice-Boltzmann method (LBM) employed by the commercial software suite, PowerFLOW 6-2021, was used throughout this work due to its proven accuracy on similarly complex rotorcraft problems (Refs. 10, 19–21). LBM is based on kinetic theory and is explicit in nature, solving first for the convection of mesoscopic fluid particles before solving for the collision of these particles on a Cartesian mesh (i.e., lattice). In this work, a statistical description of discrete particle motion along 19 directions in 3-D space (D3Q19 stencil) was used. The general form of the lattice-Boltzmann equation, given in Refs. 22 and 23, can be seen in Eq. (4):

$$f_i(\mathbf{x} + \mathbf{e}_i \Delta x, t + \Delta t) = f_i(\mathbf{x}, t) + \Omega_i(\mathbf{x}, t), \quad (i = 0, 1, ..., 19), \tag{4}$$

where f_i is the particle velocity distribution function along the i^{th} direction, $\mathbf{x}$ is the particle position at time, t, $\mathbf{e}_i$ is the particle convective speed, which was intrinsically calculated for particles to travel one cell each time step (i.e., $|\mathbf{e}_i| = \Delta x/\Delta t$), and Ω_i is the collision operator representing the rate of change of f_i resulting from particle collision. The Bhatnagar-Gross-Krook (BGK) approximation (Ref. 24), shown in Eq. (5), was used to model the collision operator:

$$\Omega_i(\mathbf{x}, t) = -\frac{1}{\tau}[f_i(\mathbf{x}, t) - f_i^{eq}(\mathbf{x}, t)], \tag{5}$$

where τ is the viscous relaxation time, which is related to the kinematic fluid viscosity, ν, and the speed of sound, a, via the following equation:

$$\nu = a^2 \left(\tau - \frac{\Delta t}{2} \right). \tag{6}$$

Table 1: Flow conditions for 2-D viscous flow analysis.

Spanwise Location	Chord Length	Reynolds Number	Mach Number	Angle of Attack
0.75R	0.984 in	1.09 x 10^5	0.174	2.13°
0.95R	0.797 in	1.12 x 10^5	0.220	2.23°

The particle equilibrium distribution, f_i^{eq}, is approximated by a third-order expansion (Ref. 25):

$$f_i^{eq}(\mathbf{x},t) = \rho\omega_i\left(1+\frac{\mathbf{e}_i\mathbf{u}}{T_0}+\frac{(\mathbf{e}_i\mathbf{u})^2}{2T_0^2}-\frac{\mathbf{u}^2}{2T_0}+\frac{(\mathbf{e}_i\mathbf{u})^3}{6T_0^3}-\frac{(\mathbf{e}_i\mathbf{u})\mathbf{u}^2}{2T_0^2}\right), \tag{7}$$

where ρ is the fluid density, ω_i is a weight function dependent on direction, $\mathbf{u}$ is the fluid velocity, and $T_0 = 1/3$ is the isothermal fluid temperature in lattice units (Ref. 26). The macroscopic fluid density and momentum can be recovered from the mesoscopic particle velocity distribution function using the Chapman-Enskog expansion (Ref. 27), which produces the following:

$$\rho = \sum_i f_i, \qquad \rho\mathbf{u} = \sum_i \mathbf{e}_i f_i. \tag{8}$$

Contrary to standard turbulence modeling procedures used by traditional Navier-Stokes solvers, which use closure models to approximate the Reynolds stress as an effective eddy viscosity contribution to the governing equations, the LBM implemented in this work used a very-large-eddy simulation (VLES) to model the unresolved, subgrid turbulence. The VLES process entailed the recalibration of τ using a turbulent relaxation time calculated via a two-equation $k-\varepsilon$ renormalization group (RNG) (Ref. 28). The resultant relaxation time, τ_{eff}, is of the form:

$$\tau_{eff} = \tau + C_\mu \frac{k^2/\varepsilon}{\sqrt{1+\eta^2}}, \tag{9}$$

where $C_\mu = 0.09$ and η is a combination of the local turbulence parameters: strain, vorticity, and helicity (Refs. 29, 30).

PowerFLOW employs an immersed boundary method to reduce the number of near-body volumetric cells (i.e, voxels), which eliminates the need for body-fitted, stretched boundary layer grids like those commonly associated with traditional Navier-Stokes solvers. This method uses a particle bounce-back algorithm at the geometry boundary to achieve a no-slip wall condition (Ref. 31). To further reduce computational cost, three types of boundary layer wall-functions can be specified for use in the first voxel adjacent to the geometry. The fully laminar and fully turbulent wall-functions follow the well-known, law-of-the-wall for laminar or turbulent flow with a modification to allow for pressure gradient effects (Ref. 30). The transitional wall-functions, on the other hand, sample the turbulent kinetic energy from the flowfield outside of the first cell adjacent to the geometry where the wall-functions are used. This sampled turbulent kinetic energy is compared to a value computed using turbulent wall shear stress from the law-of-the-wall. If the sampled values are larger than the computed turbulent kinetic energy, then the boundary layer is assumed to be turbulent and the correspondent turbulent wall shear stress is used; otherwise, a laminar wall shear stress is used. This procedure is performed at each time step, meaning that the laminar-to-turbulent transition location is time-dependent. This approach has been patented as US 2014/0136159 A1 (Ref. 32) and its accuracy in predicting the laminar-to-turbulent transition location when compared with experimental results has been shown by Duda et al. (Ref. 33). Since this methodology uses sampled turbulent flow properties as opposed to the inclusion of additional transport equations, upstream turbulence information is not locally available, meaning these transitional wall-functions are incapable of predicting laminar separation bubbles, bypass transition, and cross-flow transition (Ref. 33).

High-Fidelity Computational Strategy

The computational domain for each of the three LBM-VLES simulations was automatically discretized within PowerFLOW 6-2021 using purely hexahedron cells (i.e., voxels) in a similar fashion to what was done in Thurman et al. (Refs. 10,19), which can be seen in Fig. 7. The boundary of two adjacent variable resolution (VR) regions contains hanging nodes, where the voxels in the coarser region are twice as large as the voxels in the adjacent, finer region, which can be seen in Fig. 7c. A cuboidal computational domain extending appromixately $50R$ away from the center of the rotor in all directions was used throughout this work with a cylindrical VR region dedicated to resolving the rotor wake extending $2.25R$ away from the center of the rotor, shown in Figs. 7a and 7b, respectively.

A series of seven spheres surrounding the rotor wake VR were also defined, growing outward toward the cuboidal computational domain extents to gradually decrease the spatial resolution. The finest voxel size in the VR adjacent to the rotor, Δs, was defined to be $c_{\text{tip}}/400$. The dimensional value of this finest voxel size and correspondent y^+ values calculated using Eq. (10) at the $r = 0.5R$, $r = 0.75R$, and $r = R$ spanwise locations have been tabulated in Table 2;

$$y^+ = \frac{\Delta s U_{fric}}{\nu}, \quad U_{fric} = \sqrt{\frac{\tau_{wall}}{\rho}}, \quad \tau_{wall} = \frac{C_f \rho (r\Omega R)^2}{2}, \quad C_f = \frac{0.026}{Re_r}, \quad Re_r = \frac{(r\Omega R)c_r}{\nu}, \tag{10}$$

where c_r is the chord length at the r spanwise location.

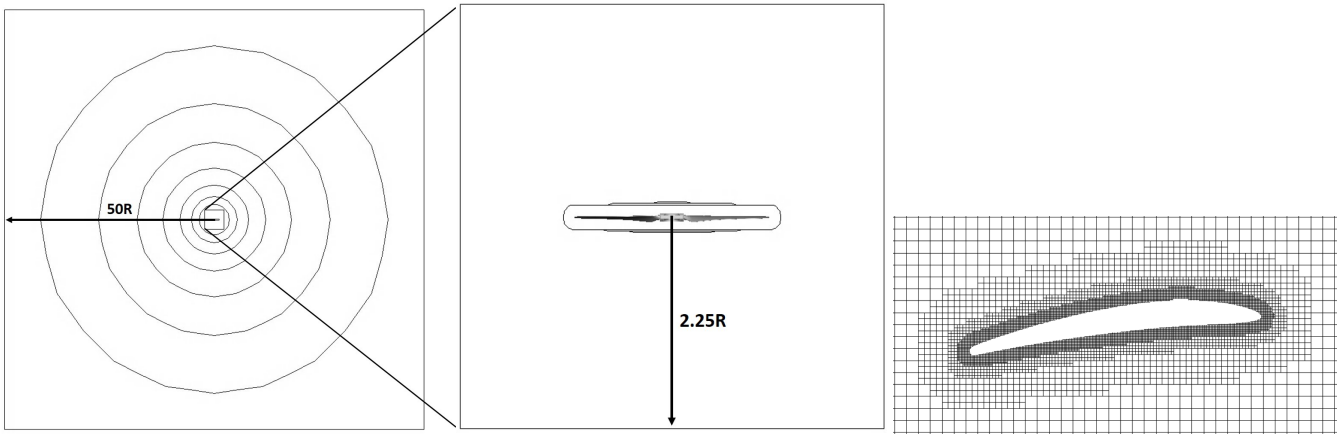

(a) Full computational domain. (b) Dedicated wake resolution region. (c) Near-field resolution along rotor blade.

Figure 7: High-fidelity computational domain visualization.

Table 2: Finest voxel size attributes.

Spanwise Location	c_r (in)	y^+	Voxel Size (in)	Voxel Size (%c_{tip})
0.50R	1.22	6.52		
0.75R	0.984	9.65	0.001875	0.25
R	0.75	12.8		

A VR region containing the rotor geometry and first three VR regions, shown in Fig. 7b, was also defined with a rotational speed equivalent to the rotor speed of $\Omega = 3950$ RPM and interpolation was used between this rotational VR region and the adjacent stationary computational domain. A no-slip boundary condition was imposed on the rotor and hub surfaces and STP conditions, as well as a zero velocity condition, were imposed on the outer cuboidal boundaries of the computational domain. Three simulations, the NT, PT, and FT cases, were performed in this work with the intent of predicting broadband LBL-VS noise or its absence from the three different blade types: SLA-smooth, SLA-tripped, and SLS, respectively. A summary of the wall-functions used for each case and the correspondent blade type being simulated is shown in Table 3 for clarity. Flowfield convergence was determined to occur at the eighth simulated rotor revolution, so each simulation was conducted over nineteen rotor revolutions, with the last ten being used for acoustic data analysis.

Acoustic Post-Processing

Unsteady blade loading was sampled over the last ten predicted rotor revolutions at a rate of 133 kHz. These sampled data were then provided to PowerACOUSTICS 6-2021 for the computation of propagated APTH at defined observer locations using a forward-time implementation of Farassat's F1A (Ref. 34). Since unsteady loading directly on the blade surfaces was used for this acoustic calculation, it is considered an *impermeable* formulation.

For the experimentally acquired APTH, care was taken to ensure data acquisition prior to the onset on flow recirculation, as discussed in Pettingill et al. (Ref. 9). An average of approximately 320 revolutions of APTH data were acquired over all three experimental cases, which will be used as the metric for subsequent experimental post-processing discussion; however, it should be noted that experimental post-processing was conducted over the respective number of acquired revolutions of APTH data for each case.

The ten revolutions of predicted APTH data and the 320 revolutions of experimentally measured APTH data were separated into ten and 320 equally sized partitions, respectively, correspondent to each revolution of rotor data. These revolutions of data were averaged together to obtain a mean revolution of APTH, which is the periodic (i.e., tonal) noise signal. This tonal noise component was then subtracted from the raw, aperiodic APTH from the ten and 320 revolutions of APTH data for the prediction and experiment, respectively, and the resultant residual APTH served as the stochastic (i.e., broadband) noise signal. This technique for periodic averaging and broadband noise extraction has been applied extensively to both experimental and computational data with great success in previous work (Refs. 9, 10, 19, 35, 36).

The mean rotor revolution of predicted data was repeated enough times to attain a $\Delta f = 20$ Hz frequency resolution, which was then processed by treating the repeated rotor revolution data as an aperiodic signal, computing the fast Fourier Transform (FFT) of the data, then using Eq. (11) to produce a narrowband spectrum of the predicted tonal noise sound pressure level (SPL);

$$\text{SPL} = 10\log_{10}\left(\frac{P_{xx} * \Delta f}{p_{ref}^2}\right), \tag{11}$$

Table 3: High-fidelity simulation summary.

Simulation Case	Blade Type	Wall-functions
Natural transition (NT)	SLA-smooth	Transitional
Physical trip (PT)	SLA-tripped	Transitional with turbulent downstream of trip on suction side
Fully turbulent (FT)	SLS	Turbulent

where P_{xx} is the resultant power spectral density from the FFT calculation and $p_{ref} = 20\ \mu$Pa. A similar approach was taken for the tonal noise component of the experimetally acquired data.

The extracted broadband noise signal from both the computations and experiment were treated as aperiodic signals over which an FFT was also calculated with bin widths of $\Delta f = 50$ Hz and $\Delta f = 20$ Hz, respectively. The larger bin width was required for the computational data due to the limited revolutions of APTH data. Equation (11) was used to produce narrowband broadband noise SPL values, which were then used to generate one-third octave band ($SPL_{1/3}$) representations. A logarithmic representation of the resultant computational and experimental broadband P_{xx} values from the FFT calculation were also generated using the following:

$$\text{PSD} = 10\log_{10}\left(\frac{P_{xx}}{p_{ref}^2}\right). \tag{12}$$

These tonal and broadband noise post-processing techniques were used on APTH data at an observer location correspondent to M6 ($\Theta_{obs} = -35°$, $y = 7.5$ ft) in Fig. 5, which will be referred to as the out-of-plane observer location.

AERODYNAMIC RESULTS

The computational and experimental thrust values of the three simulations and blade types at the design operating condition are shown in Table 4. It can be seen that the measured thrust was lower for the SLA-tripped and SLS blades when compared to the SLA-smooth blades. This trend is in agreement with results from Traub (Ref. 37) and Sreejith and Sathyabhama (Ref. 38), where tripping an airfoil boundary layer had the effect of reducing the generated lift. The simulated results from the PT and FT cases compare well to the experimental data; however, the results from the NT case are underpredicted by 14%.

The underprediction from the NT case when compared to the FT case can be explained by comparing the surface pressure data at the $0.75R$ spanwise location between both cases. Looking at Fig. 8, it can be seen that there is a large suction pressure region on the pressure side of the blades in the trailing edge vicinity. This region is present for both the NT and FT cases, with the NT case having a higher associated suction pressure, which could contribute to the thrust underprediction from the NT case. Since PowerFLOW samples surface quantities from the fluid region adjacent to the geometry, this suction pressure region could be attributed to flow separation or vortex shedding around the thick, rounded trailing edge of

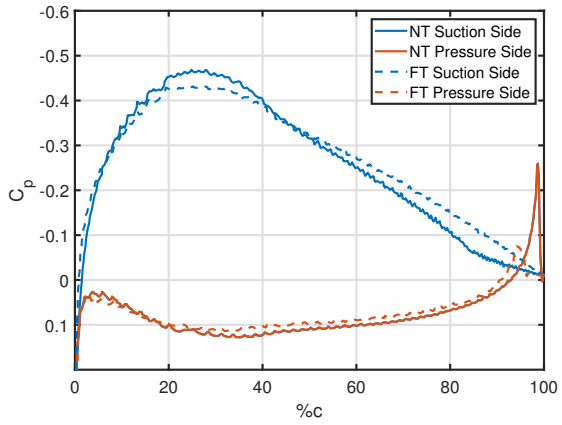

Figure 8: Pressure distribution for the NT and FT PowerFLOW simulation cases at the $0.75R$ spanwise location.

the cambered rotor blades. The higher shear stress associated with turbulent wall-bounded flow would mitigate this behavior when compared to a laminar or transitional case, possibly explaining the trailing edge suction pressure differences between the NT and FT cases shown in Fig. 8.

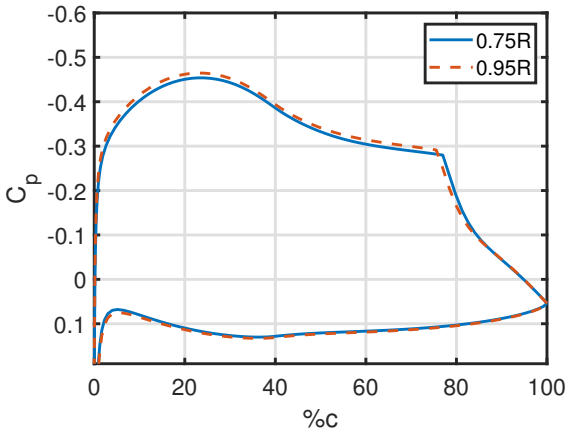

Figure 9: Pressure distribution calculated using XFOIL at the $0.75R$ and $0.95R$ spanwise locations.

Pressure distributions from the low-fidelity 2-D viscous flow prediction tool, XFOIL, at the $0.75R$ and $0.95R$ spanwise locations are also shown in Fig. 9 for an NACA 5408 airfoil with closed trailing edge, using the characteristic flow quantities shown in Table 1. This figure shows a pressure 'shelf' indicative of a laminar separation bubble occurring between approximately 50% and 80% chord for both spanwise locations, validating the assumed transitional boundary layer character of the SLA-smooth blades. This behavior is characteristic of

Table 4: Dimensional thrust comparison.

Simulation Case	Blade Type	Measured Thrust (lb)	Predicted Thrust (lb)	Relative Error (%)
NT	SLA-smooth	1.86	1.60	14.0
PT	SLA-tripped	1.74	1.72	1.17
FT	SLS	1.75	1.71	2.29

what one would expect from a transitioning boundary layer and the differences between Fig. 9 and the NT case in Fig. 8 prove that the transitional wall-functions in PowerFLOW are incapable of predicting all correspondent flow physics associated with the transition process; in this case, laminar separation bubbles. Since a region of separated flow over the blades from laminar separation bubbles would reduce the lift generated by a blade section and consequently the thrust generated by the rotor, it can be concluded that this misprediction is not responsible for the underprediction of thrust from the NT case, shown in Fig. 4.

Dimensionless skin friction, C_f, values have also been calculated over the blade geometry for the NT case and are depicted in Fig. 10, which shows a notable boundary layer transition occurring near the trailing edge of the blade. This transition location corresponds with the slight 'kink' in the NT pressure distribution shown in Fig. 8 occuring around 80% chord. This elucidates that although PowerFLOW fails to simulate all correspondent flow physics associated with the transition process, which degrades the aerodynamic performance accuracy, it is still able to reasonably predict the location of boundary layer transition when compared with the turbulent reattachment point predicted by XFOIL at around 80% chord shown in Fig. 9.

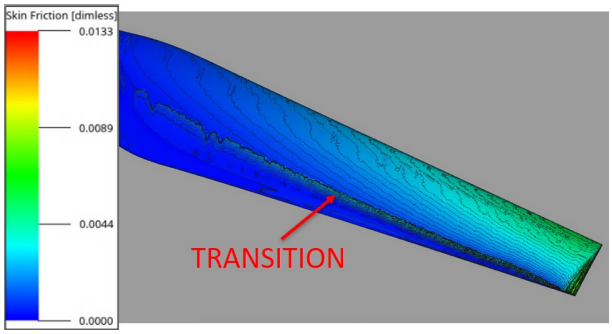

Figure 10: Dimensionless skin friction for the NT PowerFLOW simulation case.

AEROACOUSTIC RESULTS

Experimental Results

Experimental total noise narrowband spectra at the out-of-plane observer location were calculated using the raw APTH data using Eq. (11) and are shown for all three blade types in Fig. 11.

From this figure, the following observations can be made:

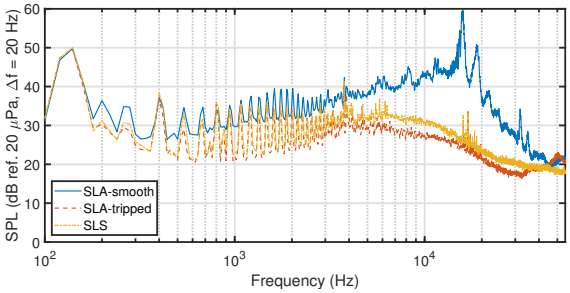

Figure 11: Experimental total noise narrowband spectra at the out-of-plane observer location ($\Theta_{obs} = -35°$, $y = 7.5$ ft).

1. All three blade types produce approximately the same tonal amplitude at the fundamental BPF and, to a lesser extent, its second harmonic at approximately 132 Hz and 264 Hz, respectively, which is in contrast to what one would expect, considering the differing experimental thrust values shown in Table 4. This behavior indicates that the tonal noise is dominated by the thickness noise (i.e., geometry dependent) component as opposed to the loading noise (i.e., force dependent) component, comparable to what was seen in Pettingill et al. (Ref. 9) for a similar canonical rotor.

2. The SLA-smooth blades exhibit pronounced LBL-VS noise around 16 kHz, denoted by the tonal peak surrounded by "ladder-like" secondary tones (Ref. 7).

3. The SLA-tripped and SLS blades effectively mitigated this LBL-VS noise, with the mid-frequency broadband shelf of the SLS blades (between 3 kHz and 16 kHz), being a bit higher than for the SLA-tripped blades. This is thought to be due to the additional turbulent flow over the pressure side of the SLS blades, which is absent for the SLA-tripped blades.

4. A broadband noise decrease of approximately 30 dB at the frequency of maximum noise emmision can be attained by either tripping the suction side of the blades or by using fabrication materials with added surface roughness.

Computational Tonal Noise Results

Tonal noise levels for all three high-fidelity simulations are compared against their respective experimental counterparts at the out-of-plane observer location on an SPL basis in Fig. 12. From this figure, it can be seen that all three computational cases predict the fundamental BPF reasonably well, with a

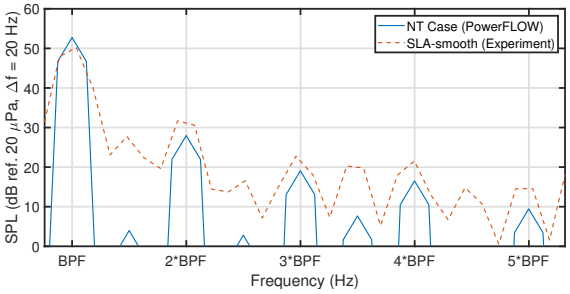

(a) PowerFLOW NT case vs. SLA-smooth experiment.

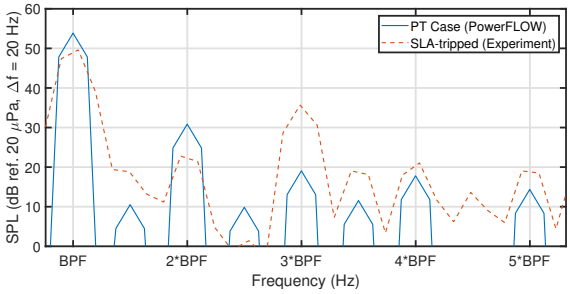

(b) PowerFLOW PT case vs. SLA-gritted experiment.

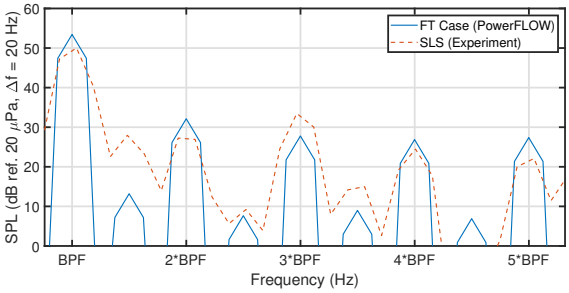

(c) PowerFLOW FT case vs. SLS experiment.

Figure 12: Tonal noise narrowband spectra at the out-of-plane observer location ($\Theta_{obs} = -35°$, $y = 7.5$ ft).

slight overprediction. To physically set the collective pitch, $\theta_0 = 0°$, of the rotor blades in the experiment, a peripheral apparatus was fit to the blades, which used an inclinometer for measurement. This rudimentary approach has associated uncertainty, and though the tonal noise is dominated by the thickness noise component, changes in θ_0 have been shown to vary the tonal noise amplitudes (Ref. 10). This uncertainty associated with physically setting θ_0 could very well be responsible for the slight overprediction from the computational results.

It is interesting to note the prediction accuracy of the fundamental BPF harmonic for the NT case shown in Fig. 12a, considering the drastic underprediction of thrust for this case when compared to the experimental SLA-smooth value, shown in Table 4. Looking at Fig. 12b, it can be seen that the PT simulation overpredicted the fundamental BPF by approximately 4 dB from the SLA-tripped experiment, which is a larger discrepancy than for the NT and FT cases. It is thought that this phenomena is due to the increased blade thickness resulting from modeling the boundary layer trip.

Computational Broadband Noise Results

Broadband noise levels for the NT, PT, and FT computational cases have been plotted against their experimental counterparts on both a PSD basis as well as a one-third octave basis in Figs. 13, 14, and 15, respectively. Looking at Fig. 13, it can be seen that the predicted broadband noise results are drastically underpredicted when compared to the SLA-smooth experimental results. Though the trend is predicted accurately, the predicted amplitudes are approximately 10 dB below the experimental results up to 5 kHz, after which, this deviation increases.

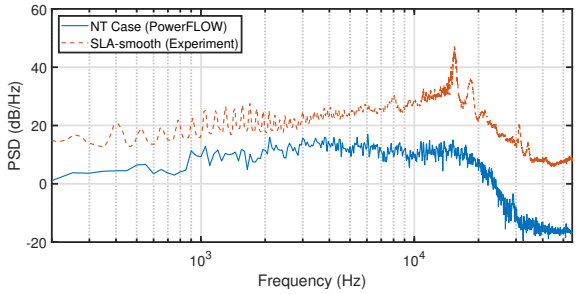

(a) Broadband noise narrowband spectra.

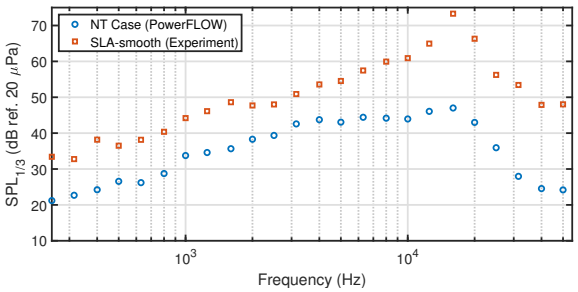

(b) Broadband noise one-third octave spectra.

Figure 13: PowerFLOW NT case vs. SLA-smooth experiment at the out-of-plane observer location ($\Theta_{obs} = -35°$, $y = 7.5$ ft).

Figure 13b does show that the simulation captured a slight tonal peak at approximately 16 kHz, which is roughly the

same frequency for which LBL-VS noise is seen for the experimental results. Since no laminar separation bubble was predicted by PowerFLOW, based on the findings from the Aerodynamic Results section, there would be no associated vortices shedding past the blade trailing edges implying the solver's inability to predict LBL-VS noise. The overall trend of this broadband noise underprediction with a high frequency tonal amplitude is similar to what was seen for a coarse spatial resolution case during a grid refinement study performed by Thurman et al. (Ref. 13). For these reasons, it is believed that this predicted tonal peak around 16 kHz for the NT case may be due to inadequate spatial resolution in the computational domain for a transitional flow regime of this type.

The broadband noise results for the PT case in Fig. 14 show excellent agreement with the SLA-tripped experimental results up to approximately 40 kHz. Since the boundary layer is physically being tripped at the quarter chord blade location, the resulting turbulent boundary layer would be more developed than for the NT case, which was shown to transition around approximately 80% chord in Figs. 8 and 10. A mature turbulent boundary layer traversing the trailing edge of a blade would have more energetic (i.e., noise producing) turbulence when compared to a recently transitioned turbulent boundary layer, which could explain the increase in higher-frequency broadband noise levels for the PT case when compared to the NT case.

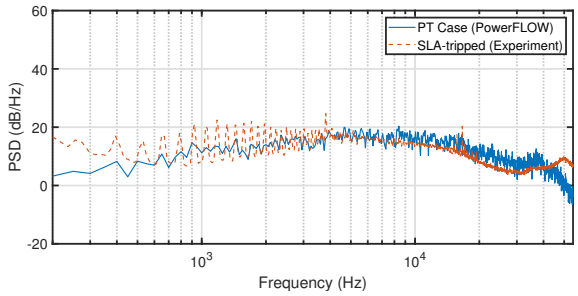

(a) Broadband noise narrowband spectra.

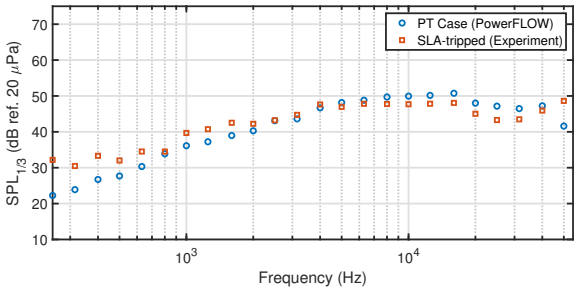

(b) Broadband noise one-third octave spectra.

Figure 14: PowerFLOW PT case vs. SLA-tripped experiment at the out-of-plane observer location ($\Theta_{obs} = -35°$, $y = 7.5$ ft).

Figure 15 shows the predicted results from the FT case compared with the SLS experimental results. Excellent agreement can be seen up to approximately 5 kHz, after which, the computed results decrease significantly away from the experimental results. It is well-known that all turbulent boundary layers undergo a transition process with surface roughness effects moving the transition location further upstream. Treating the boundary layer as fully turbulent across the entirety of the rotor may not have been a suitable prediction approach, which could be responsible for the underprediction above 5 kHz. Additionally, adding surface roughness effects to the boundary condition on the rotor surface could increase the higher-frequency broadband noise, similar to what was seen in Cheng et al. (Ref. 39), leading to more accurate predictions.

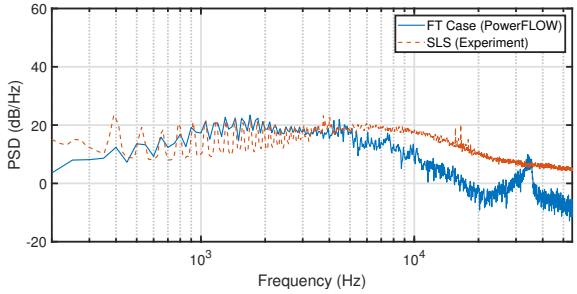

(a) Broadband noise narrowband spectra.

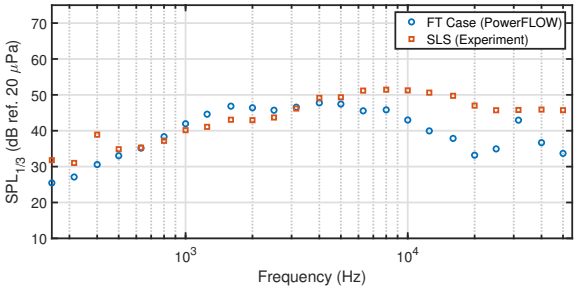

(b) Broadband noise one-third octave spectra.

Figure 15: PowerFLOW FT case vs. SLS experiment at the out-of-plane observer location ($\Theta_{obs} = -35°$, $y = 7.5$ ft).

CONCLUSIONS AND FUTURE WORK

This work investigated the effect of a rotor blade's boundary layer on the broadband LBL-VS self-noise emitted from an optimum hovering rotor. First, an experimental study was performed using three types of rotor blades with varying surface roughness dictated by the manufacturing technique utilized or with the addition of a boundary layer trip. This experimental study showed that rotors with blades having turbulent boundary layers (caused by a boundary layer trip or by surface roughness effects), produced less thrust than with blades having laminar-to-turbulent transitioning flows. It was shown that regardless of the measured thrust differences between blade types, the tonal noise was largely thickness noise (i.e., geometry) dominant and the tonal noise amplitudes at the fundamental and second harmonic of the BPF showed negligible differences between blade types. This was in contrast to the broadband noise, which exhibited substantial differences based upon blade type. The smoothest blades (SLA-smooth) were shown to have a laminar-to-turbulent transi-

tional boundary layer, which produced a large tonal amplitude in the broadband noise signature at approximately 16 kHz, surrounded by secondary "ladder-like" tones, which is characteristic of LBL-VS broadband noise. This experimental work showed that surface roughness effects or the addition of a boundary layer trip serve to mitigate this LBL-VS noise by upward of 30 dB at the frequency of maximum noise emission, with the boundary layer trip further reducing the broadband noise between 3 kHz and 16 kHz when compared to the blades with surface roughness effects.

A multifidelity computational study was also performed in this work. The low-fidelity 2-D viscous flow prediction tool, XFOIL, was used to verify the presence of laminar separation bubbles causing LBL-VS noise at the $0.75R$ and $0.95R$ spanwise locations using characteristic flow properties calculated using ANOPP's PAS. The high-fidelity lattice-Boltzmann code, PowerFLOW 6-2021, was also used to simulate the three blade types using different wall-functions to dictate the boundary layer behavior. The high-fidelity simulation with laminar-to-turbulent transitional wall-functions showed a thrust underprediction of 14% when compared to its experimental counterpart. This simulation also showed accurate tonal noise prediction and broadband noise trend; however, the broadband noise was underpredicted by approximately 10 dB up to 5 kHz, after which, the deviation increased. The thrust underprediction was shown to be the result of flow separation on the pressure side of the blades, which had negligible impact on the tonal noise comparison, whereas the drastic broadband noise underprediction was thought to result from inadequate spatial resolution in the computational domain. The simulation involving physically modeling the boundary layer trip showed excellent agreement in thrust, tonal noise, and broadband noise up to 40 kHz when compared to its experimental counterpart. Lastly, the simulation using fully turbulent wall-functions showed excellent agreement in thrust and tonal noise when compared to blades with surface roughness effects; however, the broadband noise was only predicted accurately up to 5 kHz. It is believed that adding surface roughness effects to the fully turbulent wall-functions could increase the higher-frequency broadband noise and lead to more accurate predictions.

It can be concluded from this work that a rotor blade's boundary layer character can be modified to reduce the broadband noise at the cost of slightly decreased aerodynamic performance and that the current high-fidelity simulations conducted using PowerFLOW 6-2021 may only provide accurate broadband noise predictions for certain flow conditions. More research is necessary to determine the suitability of using lattice-Boltzmann simulations and more specifically, different wall-functions, for predicting broadband noise caused by different boundary layer regimes. Future work will include a grid resolution study and the addition of varying levels of surface roughness to the wall-functions for more accurate broadband noise prediction.

Author contact: Christopher S. Thurman,
christopher.thurman@nasa.gov

ACKNOWLEDGMENTS

This work was funded by the NASA Revolutionary Vertical Lift Technology (RVLT) project. Computational resources supporting this work were provided by the NASA High-End Computing (HEC) Program through the NASA Advanced Supercomputing (NAS) Division at Ames Research Center.

REFERENCES

1. Paterson, R. W., Vogt, P. G., Fink, M. R., and Munch, C. L., "Vortex Noise of Isolated Airfoils," *Journal of Aircraft*, Vol. 10, (5), 1973, pp. 296–302.

2. Arbey, H., and Bataille, J., "Noise Generated by Airfoil Profiles Placed in a Uniform Laminar Flow," *Journal of Fluid Mechanics*, Vol. 134, 1983, pp. 33–47.

3. Plogmann, B., Herrig, A., and Würz, W., "Experimental Investigations of a Trailing Edge Noise Feedback Mechanism on a NACA 0012 Airfoil," *Experiments in Fluids*, Vol. 54, (5), 2013.

4. Pröbsting, S., Scarano, F., and Morris, S. C., "Regimes of Tonal Noise on an Airfoil at Moderate Reynolds Number," *Journal of Fluid Mechanics*, Vol. 780, 2015, pp. 407–438.

5. Jones, L. E., Sandberg, R. D., and Sandham, N. D., "Direct Numerical Simulations of Forced and Unforced Separation Bubbles on an Airfoil at Incidence," *Journal of Fluid Mechanics*, Vol. 602, 2008, pp. 175–207.

6. Ricciardi, T. R., Ribeiro, J. H. M., and Wolf, W., "Analysis of Coherent Structures in Large-eddy Simulations of a NACA0012 Airfoil," AIAA Scitech 2019 Forum, San Diego, CA, 2019.

7. Ricciardi, T. R., Wolf, W., and Taira, K., "Laminar-turbulent Transition and Intermittency Effects on Secondary Tones from a NACA0012 Airfoil," AIAA Aviation 2021 Forum, Virtual, August 2021.

8. Brooks, T. F., Pope, D. S., and Marcolini, M. A., "Airfoil Self-Noise and Prediction," NASA RP 1218, 1989.

9. Pettingill, N. A., Zawodny, N. S., Thurman, C. S., and Lopes, L. V., "Acoustic and Performance Characteristics of an Ideally Twisted Rotor in Hover," AIAA SciTech 2021 Forum, Virtual, January 2021.

10. Thurman, C. S., Zawodny, N. S., Pettingill, N. A., Lopes, L. V., and Baeder, J. D., "Physics-informed Broadband Noise Source Identification and Prediction of an Ideally Twisted Rotor," AIAA SciTech 2021 Forum, Virtual, January 2021.

11. Lopes, L. V., and Burley, C. L., "ANOPP2 User's Manual: Version 1.2," NASA TM 2016-219342, 2016.

12. Leishman, J. G., *Principles of Helicopter Aerodynamics*, Cambridge University Press, New York, NY, 2000.

13. Thurman, C. S., and Zawodny, N. S., "Aeroacoustic Characterization of Optimum Hovering Rotors using Artificial Neural Networks," VFS International 77th Annual Forum & Technology Display, Virtual, May 2021.

14. Stephenson, J. H., Weitsman, D., and Zawodny, N. S., "Effects of Flow Recirculation on Unmanned Aircraft Systems (UAS) Acoustic Measurements in Closed Anechoic Chambers," *The Journal of the Acoustical Society of America*, Vol. 145, (3), 2019, pp. 1153–1155.

15. Nguyen, L. C., and Kelly, J. J., "A Users Guide for the NASA ANOPP Propeller Analysis System," NASA CR 4768, 1997.

16. Mack, L. M., "Transition and Prediction of Broadband Noise for a Small Quadcopter," AGARD Report CP224, 1977.

17. Farassat, F., "Derivation of Formulations 1 and 1A of Farassat," NASA TM 2007-214853, 2007.

18. Ffowcs Williams, J. E., and Hawkings, D. L., "Sound Generated by Turbulence and Surfaces in Arbitrary Motion," *Philosophical Transactions of the Royal Society*, Vol. A264, (1151), 1969, pp. 321–342.

19. Thurman, C. S., Zawodny, N. S., and Baeder, J. D., "Computational Prediction of Broadband Noise from a Representative Small Unmanned Aerial System Rotor," VFS International 76th Annual Forum & Technology Display, Virtual, October 2020.

20. Nardari, C., Casalino, D., Polidoro, F., Coralic, V., Brodie, J., and Lew, P., "Numerical and Experimental Investigation of Flow Confinement Effects in UAV Rotor Noise," 25th AIAA/CEAS Aeroacoustics Conference, Delt, The Netherlands, May 2019.

21. Casalino, D., Grande, E., Romani, G., Ragno, D., and Avallone, F., "Definition of a Benchmark for Low Reynolds Number Propeller Aeroacoustics," *Aerospace Science and Technology*, Vol. 113, (106707), 2021.

22. Chen, H., Teixeira, C., and Molvig, K., "Digital Physics Approach to Computational Fluid Dynamics: Some Basic Theoretical Features," *International Journal of Modern Physics C*, Vol. 8, (4), 1997, pp. 675–684.

23. Chen, S., and Doolen, G. D., "Lattice Boltzmann Method for Fluid Flows," *Annual Review of Fluid Mechanics*, Vol. 30, 1998, pp. 329–365.

24. Bhatnagar, P. L., Gross, E. P., and Krook, M., "A Model for Collision Processes in Gases. I. Small Amplitude Processes in Charged and Neutral One-Component Systems," *Journal of Statistical Physics*, Vol. 94, (3), 1954, pp. 511–525.

25. Fan, H., Zhang, R., and Chen, H., "Extended Volumetric Scheme for Lattice Boltzmann Models," *Physical Review E*, Vol. 73, (066708), 2006.

26. Chen, H., and Teixeira, C., "H-Theorem and Origins of Instability in Thermal Lattice Boltzmann Models," *Computer Physics Communications*, Vol. 129, 2000, pp. 21–31.

27. Chapman, S., and Cowling, T., *The Mathematical Theory of Non-Uniform Gases*, Cambridge University Press, London, 1990.

28. Yakhot, V., and Orszag, S. A., "Renormalization Group Analysis of Turbulence. I. Basic Theory," *Journal of Scientific Computing*, Vol. 1, (1), 1986, pp. 3–51.

29. Lew, P., Najafi-Yazdi, A., and Mongeau, L., "Numerical Simulation of Sound from Flow over an Airfoil with a Blunt Trailing Edge," 16th AIAA/CEAS Aeroacoustics Conference, Stockholm, Sweden, June 2010.

30. Avallone, F., Casalino, D., and Ragni, D., "Impingement of a Propeller-slipstream on a Leading Edge with a Flow-permeable Insert: A Computational Aeroacoustic Study," *International Journal of Aeroacoustics*, Vol. 17, (6–8), 2018, pp. 687–711.

31. Lavallée, P., Boon, J. P., and Noullez, A., "Boundaries in Lattice Gas Flows," *Physica D: Nonlinear Phenomena*, Vol. 47, (1–2), 1991, pp. 233–240.

32. Exa Corporation, M. U., Burlington, "Computer Simulation of Physical Process Including Modeling of Laminar-to-Turbulent Transition," US 2014/0163159 A1, 2014.

33. Duda, B., Fares, E., Kotapati, R., Li, Y., Staroselsky, I., Zhang, R., and Chen, H., "Capturing Laminar to Turbulent Transition within the LBM based CFD solver PowerFLOW," AIAA Scitech 2019 Forum, San Diego, CA, 2019.

34. Casalino, D., "An Advanced Time Approach for Acoustic Analogy Predictions," *Journal of Sound and Vibration*, Vol. 261, (4), 2003, pp. 583–612.

35. Zawodny, N. S., Boyd Jr., D. D., and Burley, C. L., "Acoustic Characterization and Prediction of Representative Small-Scale Rotary-Wing Unmanned Aircraft System Components," VFS International 72nd Annual Forum & Technology Display, West Palm Beach, FL, May 2016.

36. Pettingill, N. A., and Zawodny, N. S., "Identification and Prediction of Broadband Noise for a Small Quadcopter," VFS International 75th Annual Forum & Technology Display, Philadelphia, PA, May 2019.

37. Traub, L. W., "Experimental Investigation of the Effect of Trip Strips at Low Reynolds Number," *Journal of Aircraft*, Vol. 48, (5), 2011, pp. 1776–1784.

38. Sreejith, B. K., and Sathyabhama, A., "Numerical Study on Effect of Boundary Layer Trips on Aerodynamic Performance of E216 Airfoil," *Engineering Science and*

Technology, an International Journal, Vol. 21, (1), 2018, pp. 77–88.

39. Cheng, B., Han, Y., Brentner, K. S., Palacios, J., Morris, P. J., Hanson, D., and Kinzel, M., "Surface Roughness Effect on Rotor Broadband Noise," *International Journal of Aeroacoustics*, Vol. 17, (4–5), 2018, pp. 438–466.